Check for updates

Construction of La-doped TiO$_2$@La-doped ZnO–B-doped reduced graphene oxide ternary nanocomposites for improved visible light photocatalytic activity

Mojtaba Rostami [iD] *[abc]

In this study, I demonstrated that the doping of TiO$_2$, TiO$_2$@ZnO and reduced graphene oxide (RGO) by rare earth lanthanum ion (La^{3+}) and boron (B) is an effective way to enhance photocatalytic visible light activity. The 0.02 mol% La/TiO$_2$@0.02 mol% La/ZnO, B–RGO–TiO$_2$, B–RGO-0.08% La/TiO$_2$, RGO-0.08% La/TiO$_2$@0.08% La/ZnO, and *x* mol% La/TiO$_2$@*x* mol% La/ZnO-15 wt% B–RGO (*x* = 0.04, 0.06, 0.08) ternary nanocomposites (TNCs) were prepared *via* a facile sol–gel technique. The resulting binary and ternary nanohybrid photocatalysts were used for degradation of methylene blue (MB) aqueous solution under visible light illumination as a new probe pollutant. The structure, surface morphology and area, band gap, and chemical composition of the composites were studied using scanning electron microscopy (SEM) with energy dispersive X-ray (EDX) analysis, X-ray diffraction (XRD), Fourier transform infrared (FT-IR) spectroscopy, UV-visible diffuse reflectance spectroscopy (DRS) and N$_2$ adsorption–desorption isotherm (BET) measurements. XRD results showed that 0.02 mol% La/TiO$_2$@0.02 mol% La/ZnO and *x* mol% La/TiO$_2$@*x* mol% La/ZnO-15 wt% B–RGO TNCs have anatase and wurtzite crystallites phases. The DRS analysis indicated that the absorption of the 0.08 mol% La/TiO$_2$@0.08 mol% La/ZnO-15 wt% B–RGO TNC shifted to longer wavelength regions (red shift) as well as narrower band gap. The 0.08 mol% La/TiO$_2$@0.08 mol% La/ZnO-15 wt% B–RGO TNC showed high photocatalytic decomposition of MB under visible light irradiation.

1. Introduction

Since 1972 when Fijishima *et al.* found the titanium dioxide (TiO$_2$) electrode surface phenomenon in hydrolysis, TiO$_2$ has been extensively studied as a photocatalyst by scientists from various countries.[1] Due to global air and water pollution becoming increasingly serious, the application of photocatalytic degradation of organic pollutants has attracted more and more attention.[2] Titanium dioxide is the most extensively studied photocatalyst and can degrade a variety of organic compounds.[3] However, TiO$_2$ as a photocatalyst is not widely used, mainly because ultraviolet light irradiation of TiO$_2$ can produce photo-generated electron–hole (e$^-$–h$^+$) pairs, and the light-generated e$^-$–h$^+$ pair recombination rate than pollutants adsorbed chemical reaction to be fast, photocatalytic efficiency.[4–6] Therefore, the challenge now is how to effectively prevent the electron–hole pair recombination to improve the photocatalytic

activity of TiO$_2$.[7] One strategy involves a series of modified TiO$_2$ nanocomposites, such as a noble metal deposition, doping ions, dyes or quantum dots sensitized with other compound semiconductors (*e.g.* ZnO, Nb$_2$O$_5$, WO$_3$, Cds, ZnS, *etc.*), and carbon nanostructures (such as CNTs, C60, RGO, nitrogen-doped RGO, boron-doped RGO, GQDs, nitrogen-doped GQDs, boron-doped GQDs). Among them, boron-doped RGO has large specific surface area and excellent conductivity, and its combination with TiO$_2$ to enhance photocatalytic properties has become an important research direction.[8–10] TiO$_2$, known as the most common photocatalytic material, is found in with the crystal structures rutile, anatase and brookite type and has been used in various applications depending on its nature.[11,12] Among various semiconductors, zinc oxide (ZnO) nanoparticles (NPs) have been proved to be excellent candidates because of their high photocatalytic activity for degradation of organic pollutants in water and air, use in self-cleaning surfaces, and in nano-biomedical research and drug delivery.[13]

Graphene (GR or G) or reduced graphene oxide (RGO) is a single nano-layer of sp^2 carbon atoms in a nano-hybrid two-dimensional honeycomb lattice nanostructure formation.[14,15] GR, having a large specific surface area, can significantly improve the adsorption capacity of various organic compounds.

[a]Inter Islamic Network on Science and Technology Parks in Guilan, Rasht, Iran

[b]Nanotechnology Research Centre, Nano Alvand, Simindasht Industrial Area, Karaj, Iran. E-mail: mojtaba.nanochem1@yahoo.com; Tel: +98 9394736673

[c]Research and Development Department, Cinna Gen, Simindasht Industrial Area, Karaj, Iran

In addition, GR has unique electronic properties, such as high electron mobility, and it is expected in a photocatalytic process to photo-generate electrons as effective carriers.[16–18] Results show that with mechanical or physical peeling method it is difficult to prepare GR on a large scale, and solution chemistry method can yield a good dispersion of large-scale graphene oxide (GO). However, due to the chemical method using a lot of strong oxidants, the GO surface produced has a large number of oxygen-containing functional groups (such as –COOH, –OH and epoxide), resulting in poor conductivity.[19,20] How to convert the poor conductive properties of GO into highly conductive RGO has become an important issue in current international research.[21] Recently, many researchers have used a variety of reduction methods, such as chemical reduction method, the use of certain reducing agents (*e.g.* hydrazine hydrate, sodium boron hydride, sodium citrate, vitamin C, *etc.*), thermal solvent, UV-assisted method, and photocatalytic reduction method, to effectively reduce GO to GR, which has greatly enhanced ability to transport electrons, which extends the application field of GR.[22–24] GR surface synthesized with TiO₂@ZnO can effectively prevent the agglomeration of core–shell nanoparticles, and will help improve the efficiency of TiO₂@ZnO photodegradation of organic pollutants. Since GR was discovered, because of its very good optical characteristics, it has been widely studied and applied. In particular, it has important applications in photo-catalysis, where the introduction of GR leads to a system having a higher adsorption capacity for pollutants, enhancing light absorption range to enhance the charge transfer and separation ability.[25–27] Wherein, compared to boron doped graphene with graphene undoped: can be changed the electronic properties of GR, higher conductivity, greater freedom load surface charge density, the more harmful nitrogen oxide gas adsorption, so if the B–RGO and La/TiO₂@La/ZnO complex, will have a ratio not higher B–RGO nano-composite material doped TiO₂@ZnO and photo-generated charge separation rate and stronger adsorption decomposition harmful pollutants.[28–30] Herein, a series of B–RGO based semiconducting TiO₂, La/TiO₂ and La/TiO₂@La/ZnO binary and ternary nanohybrid photocatalysts were prepared by a simple sol–gel method. The B–RGO-La/TiO₂@La/ZnO TNC photocatalyst has good photocatalytic activity under sunlight due to structural advantages and has potential application value in the fields of environmental and water remediation.

2. Experimental

2.1. Chemicals

Zinc(II) nitrate hexahydrate (Zn(NO₃)₂·6H₂O, ≥99%, M_w = 290.70 g mol⁻¹), La(NO₃)₃·6H₂O, citric acid monohydrate (C₆H₈O₇·H₂O, M_w = 208 g mol⁻¹), H₃BO₃, ethanol, and surfactant cetyltrimethylammonium bromide (CTAB) were purchased from Merck and were used without any further purification. Methylene blue (MB) (C₁₆H₁₈ClN₃S, M_w = 319.85 g mol⁻¹) was kindly provided by Alvan Co., Iran. Deionized water was prepared by an ultrapure water system (Smart-2-Pure, TKACo, Germany).

2.2. Synthesis of boron-doped RGO nano-sheet (B–RGO)

Graphene oxide was synthesized from natural graphite powder by a modification of the Hummers' process.[31] B–RGO was prepared by a hydrothermal method. 5 mL of GO was dispersed into 100 mL double distilled water and ultrasonicated for 10 min, and then 0.3 g H₃BO₃ was added to the suspension with vigorous stirring for 2 h. Then the suspension solution was transferred into a Teflon-lined stainless autoclave and heated at 200 °C for 7 h. After that, it was centrifuged at 13 000 rpm for 15 min, and washed with double distilled water and ethanol several times. Finally, the products were filtered and dried to afford B-doped RGO nano-sheet (shown in Scheme 1).

2.3. Synthesis of La/TiO₂@La/ZnO-15 wt% B–RGO ternary nanocomposites (TNCs), B–RGO–La/TiO₂, and La/TiO₂@La/ZnO core–shell nanostructures

The x mol% La-doped TiO₂ NPs were firstly synthesized by the sol–gel method.[32] A La-doped ZnO shell was coated on the La-doped TiO₂ NPs by the sol–gel method. The as-prepared La-doped TiO₂ NPs (1 g) were dispersed in a mixed solution of deionized water (200 mL), ethanol (300 mL), citric acid and CTAB (1 : 2) aqueous solution by ultrasonication for 15 min. Then, 2 g of Zn(NO₃)₂·6H₂O and x mol% La(NO₃)₃·6H₂O in deionized water (300 mL) were added dropwise to the dispersion of x mol% La-doped TiO₂ NPs under mechanical stirring. To this solution, 50 mL ethanolic solution of 15 wt% of B–RGO was added followed by sonication for 15 min to make a homogeneous suspension. Afterward, the reaction was carried out for 2 h at room temperature until it became homogeneous solution and then it was dried at 140 °C for 24 h. Finally, the obtained TNCs of La/TiO₂@La/ZnO-15 wt% B–RGO were sintered in a muffle furnace at 550 °C for 2 h (shown in Scheme 2). For comparison, the same method was used to synthesize B–RGO–La/TiO₂ and La/TiO₂@La/ZnO core–shell nanostructures without La/ZnO and B–RGO, respectively.

2.4. Characterization of the prepared nano-photocatalysts

A multiwave ultrasonic generator (Ultrasonic Technology Development Co., Iran) was used for the ultrasonic irradiation. Crystalline structure of the prepared samples was investigated by powder XRD (Philips X'pert Pro MPD, Holland) using graphite-filtered CuKα (k = 0.154 nm) radiation. The morphology was analyzed by SEM (Philips XL-30ESM, Holland) equipped with an EDX (EDX Genesis-4000, USA) facility. FT-IR spectra of the samples were recorded with a FT-IR spectrophotometer (Nicolet Magna IR 550 spectrometer, USA). Band gap measurement was conducted with a UV-visible DRS spectrophotometer (Shimadzu, model UV-3101) and dye absorption was measured using UV-visible spectroscopy (TU 1810, Electron Engineering Co., Iran). The Brunauer–Emmett–Teller (BET) specific surface areas and porosity of the samples were measured on the basis of nitrogen adsorption isotherms measured at −196 °C using a gas adsorption apparatus (Towse-e Hesgarsazan-e Asia (Sensiran), USA).
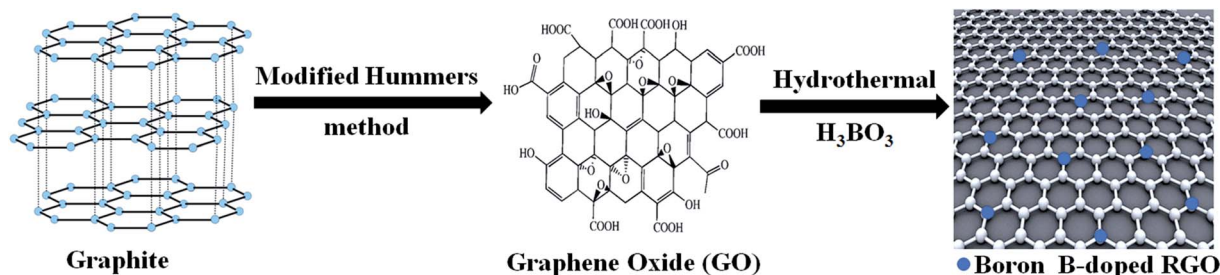
Scheme 1 Schematic procedure for preparation of boron-doped RGO nano-sheet.
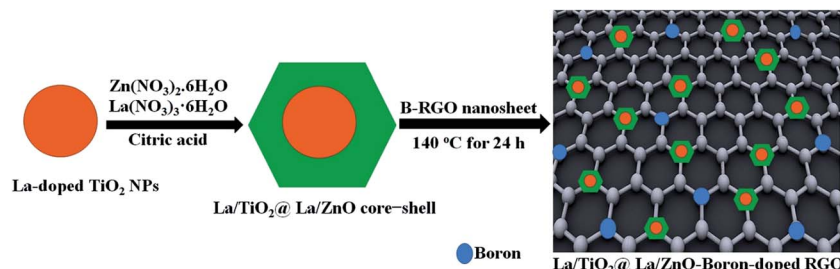
Scheme 2 Schematic procedure for preparation of La/TiO$_2$@La/ZnO–B–RGO ternary nanocomposites.

2.5. Evaluation of photocatalytic activity of the samples

Photocatalytic activities of 0.02 mol% La/TiO$_2$@0.02 mol% La/ZnO, B–RGO–TiO$_2$, B–RGO-0.08% La/TiO$_2$, RGO-0.08% La/TiO$_2$@0.08% La/ZnO, and x mol% La/TiO$_2$@x mol% La/ZnO-15 wt% B–RGO (x = 0.04, 0.06, 0.08) TNCs were evaluated by the decomposition of MB aqueous solution under visible light irradiation. Each time, 0.1 g nano-photocatalyst was dispersed into 100 mL MB aqueous solution with a concentration of 10 mg L^{-1}. The photocatalytic tests were performed in a glass vessel with a diameter of 10 cm. Then, the mixture was placed inside the photo-reactor in which the vessel was 25 cm away from the visible light sources of 400 W Osram lamps. MB oxidation experiments were carried out in a Teflon cell equipped with a quartz window. The experiments were performed at room temperature and a pH of 2.5 which was controlled once at the beginning of the experiments.

3. Results and discussion

3.1. Crystallite size and structure

XRD measurement was employed to investigate the average crystallite nano-scale and structural properties of 0.02 mol% La/TiO$_2$@0.02 mol% La/ZnO and x mol% La/TiO$_2$@x mol% La/ZnO-15 wt% B–RGO (x = 0.04, 0.06, 0.08) TNCs, as shown in Fig. 1. The peaks at 2θ values of 25.5, 37.8, 48.0, 53.9, 55.1, 62.7, 68.8, 70.3 and 75.0° can be indexed to (101), (004), (200), (105), (211), (204), (116), (220) and (215) crystal planes of anatase TiO$_2$, respectively (JCPDS card no. 21-1217). The peaks at 2θ values of 31.96, 34.65, 36.7, 47.7, 56.8, 63.1, 66.08, 68, 74.8 and 76.01° correspond to the (100), (002), (101), (102), (110), (103), (200),

(112), (201) and (202) planes of hexagonal wurtzite ZnO, respectively (JCPDS 36-1451). With a concentration of La in TiO$_2$@ZnO, the pattern showed the presence of peaks at 2θ values of 21.85, 27.81, 44.64, 58.10, and 76.10° corresponding to La$_2$O$_3$ phases.[33] The (002) peak corresponds to an interlayer distance of B–RGO nano-sheets around 26.5° as shown in Fig. 1.[34] The Debye–Scherrer equation:

$$D = \frac{k\lambda}{\beta \cos \theta}$$

was used for calculating the average crystallite size of the samples. In this equation, k is a constant which equals 0.9, λ is the wavelength of the X-ray radiation (λ = 0.154056 nm), β is the corrected band broadening (full-width at half-maximum) after subtraction of the equipment broadening, and θ is the Bragg angle.[35] The average crystallite sizes calculated for La/TiO$_2$@La/ZnO using the Debye–Scherrer equation were in the range of 170 to 200 nm.

3.2. Morphology and elemental composition

SEM was used to characterize the morphology of the samples. The SEM images for 0.02 mol% La/TiO$_2$@0.02 mol% La/ZnO core–shell nanostructure and 0.08 mol% La/TiO$_2$@0.08 mol% La/ZnO-15 wt% B–RGO TNC are shown in Fig. 2(a and b). The SEM images illustrate uniform distribution of hexagonal shape TiO$_2$@ZnO and slight agglomeration (Fig. 2(a)). As can be seen in Fig. 2(b), the almost transparent GR nano-sheets are exfoliated and approximately decorated with nearly spherical TiO$_2$@ZnO. From Fig. 2(a and b) it can be determined that the average diameter of TiO$_2$@ZnO is in the range of ~160–210 nm.

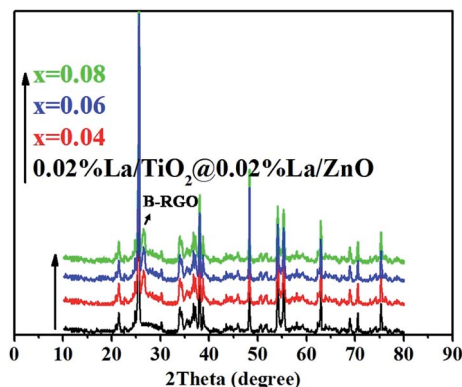EDX analysis was used to investigate the chemical composition for the constituent elements of the synthesized

Fig. 1 XRD patterns of the 0.02 mol% La/TiO$_2$@0.02 mol% La/ZnO and x mol% La/TiO$_2$@x mol% La/ZnO-15 wt% B–RGO TNCs.

0.02 mol% La/TiO$_2$@0.02 mol% La/ZnO core–shell nano-structure (Fig. 2(c)) and 0.08 mol% La/TiO$_2$@0.08 mol% La/ZnO-15 wt% B–RGO TNCs (Fig. 2(d)). The EDX analysis (Fig. 2(c and d)) exhibits the existence of Ti, Zn, C and O elements, further demonstrating the successful coating of TiO$_2$@ZnO and TiO$_2$@ZnO–B–RGO.

3.3. FT-IR spectroscopic analysis

Fig. 3 shows the FT-IR spectra for 0.02 mol% La/TiO$_2$@0.02-mol% La/ZnO and x mol% La/TiO$_2$@x mol% La/ZnO-15 wt% B–RGO (x = 0.04, 0.06, 0.08) TNCs. The C=C benzene ring skeletal stretching vibration peak could be observed around 1600 cm^{-1} for the TNC samples. The broad absorption peaks at about 3400 cm^{-1} are ascribed to the surface absorbed water or the hydroxyl groups. Graphene was also observed in that there were several peaks centered at 1568 and 2862, 2904, 1118 cm^{-1}, which were attributed to distinctive stretching vibration modes of C–C and the stretching vibration mode of C–H, respectively.[36] The characteristic absorption band at around 470–515 cm^{-1} is ascribed to the Zn–O stretching vibration.[37] In addition, the absorption signals in the range 400–800 cm^{-1} should be ascribed to the Ti–O–Ti/Ti–O–C stretching vibration.[38]

3.4. Nitrogen adsorption/desorption isotherm experiments

BET specific surface area (S_{BET}), pore volume (P_{vol}), and pore size (P_{size}) of the synthesized 0.02 mol% La/TiO$_2$@0.02 mol% La/ZnO and x mol% La/TiO$_2$@x mol% La/ZnO-15 wt% B–RGO (x = 0.04, 0.06, 0.08) TNCs were evaluated and the corresponding results are listed in Table 1. Surprisingly, the findings show that S_{BET} of the TNCs is significantly higher than that of 0.02 mol% La/TiO$_2$@0.02 mol% La/ZnO, the reason for which could be the added B–RGO nano-sheet. Table 1 indicates that 0.02 mol% La/TiO$_2$@0.02 mol% La/ZnO displays higher P_{vol} in comparison to the TNCs. With increasing amount of La rare earth, S_{BET} of the TNCs increased which was attributed to the increase of P_{vol}. According to the results in Table 1, a relatively high P_{size} was found for TNCs compared to that of 0.02 mol% La/TiO$_2$@0.02 mol% La/ZnO. Thus, it can be concluded that the prepared TNCs comprise densely packed NPs which are
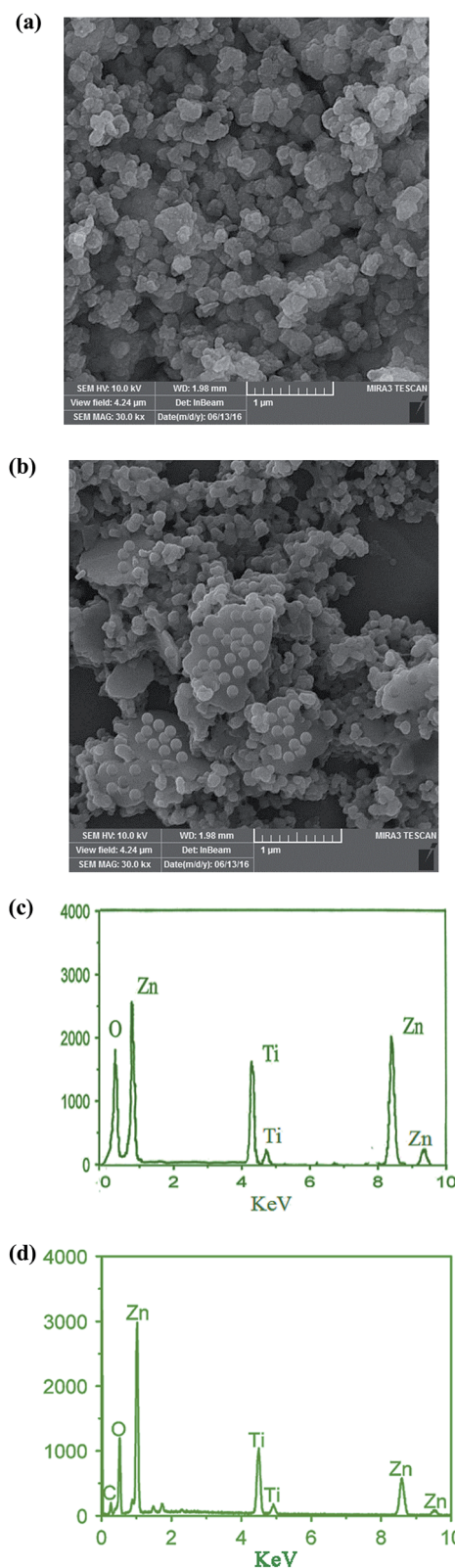

Fig. 2 SEM images of 0.02 mol% La/TiO$_2$@0.02 mol% La/ZnO (a) and 0.08 mol% La/TiO$_2$@0.08 mol% La/ZnO-15 wt% B–RGO TNCs (b). EDX spectra of the 0.02 mol% La/TiO$_2$@0.02 mol% La/ZnO (c) and 0.08 mol% La/TiO$_2$@0.08 mol% La/ZnO-15 wt% B–RGO TNCs (d).
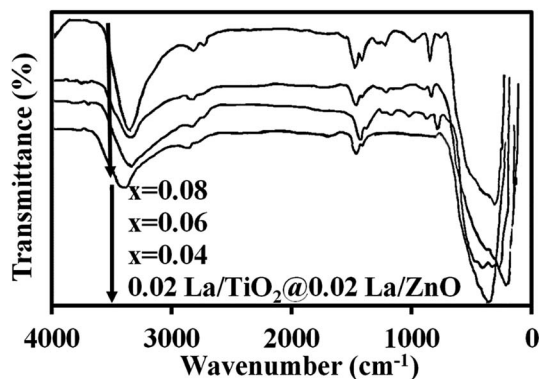
Fig. 3 FT-IR spectra of 0.02 mol% La/TiO$_2$@0.02 mol% La/ZnO and x mol% La/TiO$_2$@x mol% La/ZnO-15 wt% B–RGO TNCs.
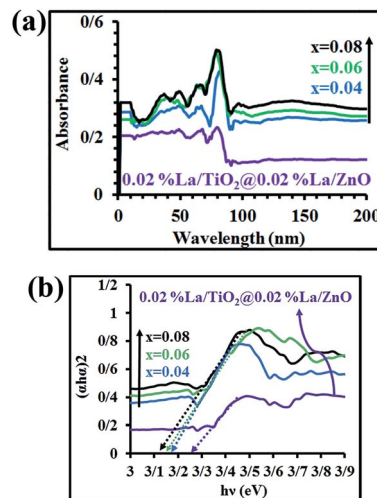

Fig. 4 (a) UV-visible diffuse reflectance spectra and (b) plots to calculate the band gap energy for 0.02 mol% La/TiO$_2$@0.02 mol% La/ZnO and x mol% La/TiO$_2$@x mol% La/ZnO-15 wt% B–RGO TNCs.

homogeneously agglomerated. Therefore, and based on the S_{BET} findings, improved photocatalytic activity of TNCs compared to 0.02 mol% La/TiO$_2$@0.02 mol% La/ZnO is expected.

3.5. Band gap analysis by UV-visible DRS

The UV-visible diffuse reflectance spectra and plots to calculate the band gap energy are illustrated in Fig. 4(a and b). The band gap of the samples was estimated using the following equation:[39]

$$(\alpha h\vartheta)^n = B_d(h\vartheta - E_g)$$

where E_g is the optical band gap of the nano-material, α is the absorption coefficient, $h\vartheta$ is the incident photon energy, and B_d is the absorption constant. The intercept of the tangent to a plot of $(\alpha h\vartheta)^2$ *versus* $h\vartheta$ gives a good approximation of the band gap energy. The estimated band gaps of 0.02 mol% La/TiO$_2$@0.02 mol% La/ZnO and x mol% La/TiO$_2$@x mol% La/ZnO-15 wt% B–RGO, $x = 0.04$, 0.06 and 0.08, were 3.27, 3.18, 3.15 and 3.12 eV, respectively. Therefore, the band gap energy was found to decrease with an increase in La doping. This band gap reduction of samples can be explained by a new energy level produced in the band gap of TiO$_2$@ZnO by the dispersion of nanoparticles in the TiO$_2$@ZnO matrix and through mixing of La 3d with Zn and Ti 3d and B and C 2p in B–RGO nano-sheet with O 2p in TiO$_2$@ZnO which leads to formation of a new conduction band (CB) and valence band (VB), respectively (shown in Scheme 3).[40] A red shift in the optical absorption edge of TNCs compared with 0.02 mol% La/TiO$_2$@0.02 mol% La/ZnO

was probably due to the chemical interaction between the B–RGO nano-sheet and semiconductor (TiO$_2$@ZnO). This red shift resulted in a narrowing of band gap energy in the TNCs resulting from the electron-accepting properties of B–RGO nano-sheets.[41]

3.6. Evaluation of the photocatalytic efficiency

Fig. 5 shows the photocatalytic degradation of MB as a function of visible light irradiation catalyzed by 0.02 mol% La/TiO$_2$@0.02 mol% La/ZnO synthesized by the sol–gel method, compared to B–RGO–TiO$_2$, B–RGO-0.08% La/TiO$_2$, RGO-0.08% La/TiO$_2$@0.08%La/ZnO, and x mol% La/TiO$_2$@x mol% La/ZnO-15 wt% B–RGO ($x = 0.04$, 0.06, 0.08) TNCs. The photocatalytic activity of the developed nano-photocatalysts was evaluated in terms of photodecomposition efficiency of MB as a new model organic pollutant using the following equation:
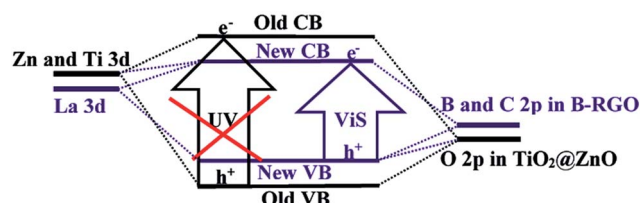
$$D\ (\%) = \left(\frac{A_o - A_i}{A_o}\right) \times 100$$

where A_o is the dark absorption of MB and A_i is the absorption of MB solution after photocatalytic decomposition under visible light irradiation.

The findings show that the photocatalytic decomposition efficiency of binary and ternary nano-hybrid photocatalysts

Table 1 S_{BET}, pore volume (P_{vol}), and pore size (P_{size}) of the synthesized samples

Sample	S_{BET} (m^2 g^{-1})	P_{vol} (cm^3 g^{-1})	P_{size} (nm)
0.02 La/TiO$_2$@0.02 La/ZnO	33	0.15	30.27
$x = 0.04$	318	0.03	4.14
$x = 0.06$	326	0.06	3.91
$x = 0.08$	332	0.11	3.53

Scheme 3 Schematic illustration of band gap narrowing mechanism of undoped and doped La/TiO$_2$@La/ZnO–B–RGO TNCs.
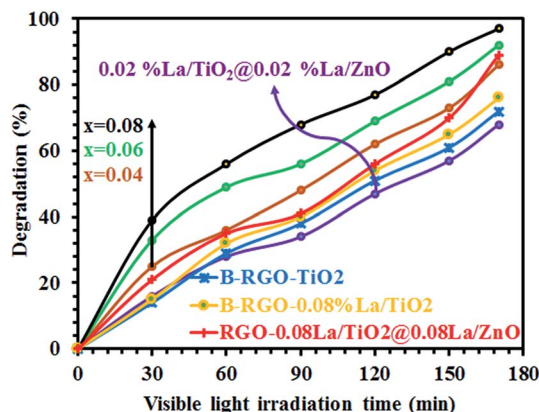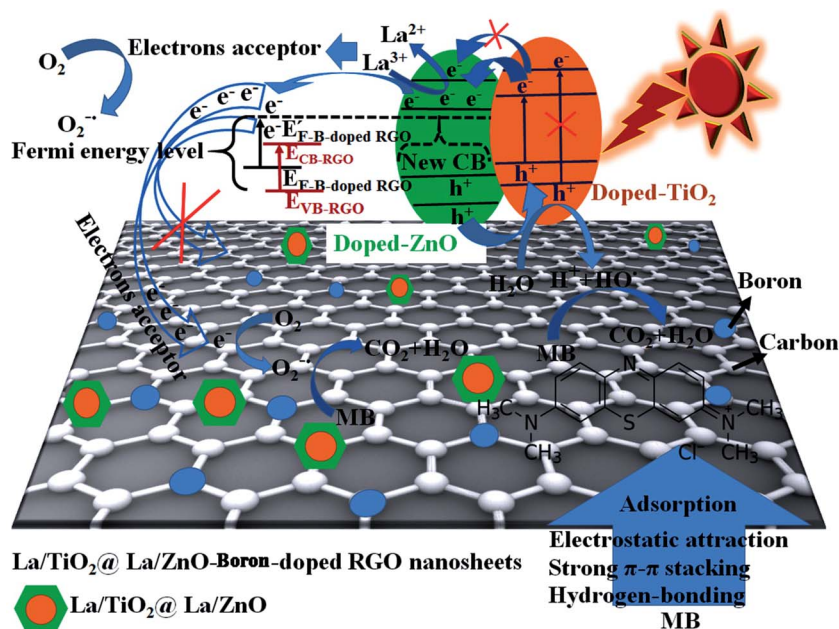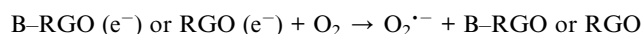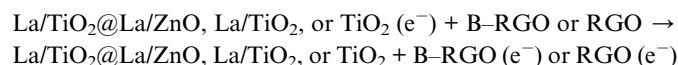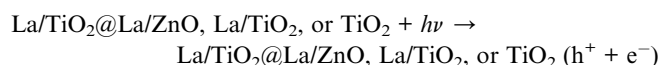
Fig. 5 Photocatalytic degradation of MB catalyzed by 0.02 mol% La/TiO$_2$@0.02 mol% La/ZnO, B–RGO–TiO$_2$, B–RGO-0.08% La/TiO$_2$, RGO-0.08% La/TiO$_2$@0.08% La/ZnO, and x mol% La/TiO$_2$@x mol% La/ZnO-15 wt% B–RGO TNCs under visible light irradiation.
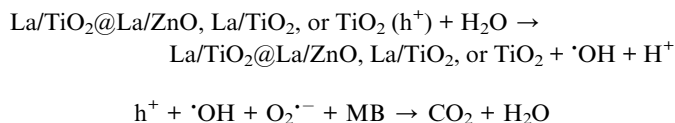
follows the order of 0.08 mol% La/TiO$_2$@0.08 mol% La/ZnO-15 wt% B–RGO (97 D%) > 0.06 mol% La/TiO$_2$@0.06 mol% La/ZnO-15 wt% B–RGO (92.1 D%) > 0.08 mol% La/TiO$_2$@0.08-mol% La/ZnO-15 wt% RGO (89.3 D%) > 0.04 mol% La/TiO$_2$@0.04 mol% La/ZnO-15 wt% B–RGO (86.1 D%) > 0.08 mol% La/TiO$_2$-15 wt% B–RGO (76.7 D%) > 0.08 mol% La/TiO$_2$-15 wt% RGO (72.6 D%) > 0.02 mol% La/TiO$_2$@0.02-mol% La/ZnO (68.5 D%). Therefore, photocatalytic performance improves with addition of lanthanum (La) and boron (B) in the binary and ternary nano-hybrid photocatalysts. The photoexcited electrons in the conduction band of ZnO can be accepted by La^{3+} and B–RGO (shown in Scheme 4).[42] Importantly, the ternary nano-hybrid photocatalysts show higher photocatalytic activity compared with binary nano-hybrid photocatalysts under visible light, benefiting from enhancement of adsorption of MB pollutants. Visible light absorption intensity improves the acceptor, transporter and delivery rate of carrier electrons, decreasing the recombination of photo-generated electrons (e$^-$) and holes (h$^+$) and more excited states of the ternary nano-hybrid photocatalysts under visible light irradiation (shown in Scheme 4).[42] The enhanced adsorptivity should be largely attributed to the hydrogen-bonding, strong π–π stacking and electrostatic attraction between MB and π-conjugation regions of the B–RGO nano-sheets (shown in Scheme 4).[43] The band gap energy of TiO$_2$ is less than that of ZnO. Therefore, when the ternary nano-hybrid photocatalysts are irradiated under visible light, the e$^-$ in the VB of TiO$_2$ are excited to the CB of ZnO. At the same time, the positive charge (h$^+$) will be left in the VB of ZnO (shown in Scheme 4).[44] The photo-generated e$^-$ of B-doped RGO make its Fermi level ($E'_{\text{F-B-doped RGO}}$) higher than the CB ($E_{\text{CB-RGO}}$) of RGO sheets (from $E_{\text{F-B-doped RGO}}$ to $E'_{\text{F-B-doped RGO}}$ in Scheme 4). The level of $E'_{\text{F-B-doped RGO}}$ just falls between the CB of ZnO and the relevant redox potentials, which is very beneficial to the transport of photo-produced electrons, as shown in Scheme 4.[45] On the basis of the above discussion, a possible mechanism for photocatalytic activity enhancement can be suggested as follows:

La/TiO$_2$@La/ZnO, La/TiO$_2$, or TiO$_2$ + $h\nu$ →
    La/TiO$_2$@La/ZnO, La/TiO$_2$, or TiO$_2$ (h$^+$ + e$^-$)

La/TiO$_2$@La/ZnO, La/TiO$_2$, or TiO$_2$ (e$^-$) + B–RGO or RGO →
La/TiO$_2$@La/ZnO, La/TiO$_2$, or TiO$_2$ + B–RGO (e$^-$) or RGO (e$^-$)

B–RGO (e$^-$) or RGO (e$^-$) + O$_2$ → O$_2^{\bullet-}$ + B–RGO or RGO

Scheme 4 Schematic diagram of proposed photocatalysis and band-gap narrowing mechanism, photo-excited and accepted electrons, adsorption of MB, and electron and hole transfer of La/TiO$_2$@La/ZnO–B–RGO TNCs under sunlight irradiation.

$$La/TiO_2@La/ZnO, La/TiO_2, \text{ or } TiO_2 (h^+) + H_2O \rightarrow$$
$$La/TiO_2@La/ZnO, La/TiO_2, \text{ or } TiO_2 + {}^{\cdot}OH + H^+$$

$$h^+ + {}^{\cdot}OH + O_2^{\cdot -} + MB \rightarrow CO_2 + H_2O$$

4. Conclusions

In conclusion, $TiO_2@ZnO$ photocatalysts consisting of La^{3+}-doped TiO_2 and ZnO nanoparticles loaded onto B–RGO nanosheets were successfully synthesized *via* a simple sol–gel method. The prepared nanoparticles were anatase and wurtzite crystallites with high photocatalytic activity under visible or solar light irradiation. The excellent electron transporting capacities of B–RGO were very beneficial to the separation of photoproduced e^-–h^+ pairs, resulting in the enhancement of photocatalytic activity under visible light irradiation and the generation of free OH and O_2 radicals. The x mol% La dopant exhibits an excellent photocatalytic activity under visible light for the degradation of MB. Finally, increasing the absorption wavelength towards the visible light region and decreasing the band gap energy in the UV-visible spectrum confirm the formation of Zn–O–C, Ti–O–C and Zn–O–Ti bonds of the synthesized nanocatalysts. Moreover, EDX spectra proved the existence of $TiO_2@ZnO$ and $TiO_2@ZnO$–B–RGO TNCs. In addition, the TNCs are very promising excellent visible-light-active photocatalysts for environmental applications such as water remediation and air purification.

Conflicts of interest

There is no conflicts of interest.

References

1 A. Fujishima and K. Honda, *Nature*, 1972, **238**, 37–38.
2 R. R. Giri, H. O. Zaki, S. Ota, R. Takanami and S. Taniguchi, *Int. J. Environ. Sci. Technol.*, 2010, **7**, 251–260.
3 M. Andersson, H. Birkedal, N. R. Franklin, T. Ostomel, S. Boettcher, A. E. C. Palmqvist and G. D. Stucky, *Chem. Mater.*, 2005, **17**, 1409–1415.
4 M. R. Elahifard, S. Rahimnejad, S. Haghighi and M. R. Gholami, *J. Am. Chem. Soc.*, 2007, **129**, 9552–9553.
5 Y. Li, H. Zhang, Z. Guo, J. Han, X. Zhao, Q. Zhao and S.-J. Kim, *Langmuir*, 2008, **24**, 8351–8357.
6 K. Awazu, M. Fujimaki, C. Rockstuhl, J. Tominaga, H. Murakami, Y. Ohki, N. Yoshida and T. Watanabe, *J. Am. Chem. Soc.*, 2008, **130**, 1676–1680.
7 J. Graciani, L. J. Alvarez, J. A. Rodriguez and J. F. Sanz, *J. Phys. Chem. C*, 2008, **112**, 2624–2631.
8 V. Subramanian, E. E. Wolf and P. V. Kamat, *J. Am. Chem. Soc.*, 2004, **126**, 4943–4950.
9 S. H. Elder, F. M. Cot, Y. Su, S. M. Heald, A. M. Tyrysgkin, M. K. Bowman, Y. Gao, A. G. Joly, M. L. Balmer, A. C. Kolwaite, K. A. Magrini and D. M. Blake, *J. Am. Chem. Soc.*, 2000, **122**, 5138–5146.
10 X. Chen, L. Liu, P. Y. Yu and S. Mao, *Science*, 2011, **331**, 746–750.
11 K. Zhou, Y. Zhu, X. Yang, X. Jiang and C. Li, *New J. Chem.*, 2011, **35**, 353–359.
12 K. Woan, G. Pyrgiotakis and W. Sigmund, *Adv. Mater.*, 2009, **21**, 2233–2239.
13 X. Zhou, X. Huang, X. Qi, S. Wu, C. Xue, F. Y. C. Boey, Q. Yan, P. Chen and H. Zhang, *J. Phys. Chem. C*, 2009, **113**, 10842–10846.
14 J. Li and C.-y. Liu, *Eur. J. Inorg. Chem.*, 2010, 1244–1248.
15 X.-Z. Tang, Z. Cao, H.-B. Zhang, J. Liu and Z.-Z. Yu, *Chem. Commun.*, 2011, **47**, 3084–3086.
16 T. Wu, S. Liu, Y. Luo, W. Lu, L. Wang and X. Sun, *Nanoscale*, 2011, **3**, 2142–2144.
17 W. S. Hummers and R. E. Offeman, *J. Am. Chem. Soc.*, 1958, **80**, 1339.
18 N. I. Kovtyukhova, P. J. Ollivier, B. R. Martin, T. E. Mallouk, S. A. Chizhik, E. V. Buzaneva and A. D. Gorchinskiy, *Chem. Mater.*, 1999, **11**, 771–778.
19 A. C. Ferrari, *Solid State Commun.*, 2007, **143**, 47–57.
20 M. Rahimi-Nasrabadi, M. Rostami, F. Ahmadi, A. Fallah Shojaei and M. Delavar Rafiee, *J. Mater. Sci.: Mater. Electron.*, 2016, **27**, 11940–11945.
21 X.-Y. Zhang, H.-P. Li, X.-L. Cui and Y. Lin, *J. Mater. Chem.*, 2010, **20**, 2801–2806.
22 N. Zhang, Y. Zhang and Y.-J. Xu, *Nanoscale*, 2012, **4**, 5792–5813.
23 F. Schedin, A. K. Geim, S. V. Morozov, E. M. Hill, P. Blake, M. I. Katsnelson and K. S. Novoselov, *Nat. Mater.*, 2007, **6**, 652–655.
24 S. Watcharotone, D. A. Dikin, S. Stankovich, R. Piner, I. Jung, G. H. B. Mommett, S. Evmenenko, S. E. Wu, S. F. Chen and C. P. Liu, *Nano Lett.*, 2007, **7**, 1888–1892.
25 T. Takamura, K. Endo, L. Fu, Y. P. Wu, K. J. Lee and T. Matsumoto, *Electrochim. Acta*, 2007, **53**, 1055–1061.
26 J. S. Lee, K. H. You and C. B. Park, *Adv. Mater.*, 2012, **24**, 1084–1088.
27 N. Zhang, Y. Zhang, X. Pan, M.-Q. Yang and Y.-J. Xu, *J. Phys. Chem. C*, 2012, **116**, 18023–18031.
28 L. Niu, L. Niu, Z. Lim, W. Hong, J. Sun, Z. Wang, L. Ma, J. Wang and S. Yang, *Electrochim. Acta*, 2013, **108**, 666–673.
29 R. Lv and T. M. Errones, *Mater. Lett.*, 2012, **78**, 209–218.
30 Y. B. Tang, L. C. Yin, Y. Yang, X. H. Bo, Y. L. Cao, H. E. Wang, W. J. Zhang, I. Bello, S. T. Lee, H. M. Cheng and C. S. Lee, *ACS Nano*, 2012, **6**, 1970–1978.
31 Y. Liang, D. Wu, X. Feng and K. Mullen, *Adv. Mater.*, 2009, **21**, 1679–1683.
32 M. Rostami, M. Rahimi-Nasrabadi, M. R. Ganjali, F. Ahmadi, A. Fallah Shojaei and M. Delavar Rafiee, *J. Mater. Sci.*, 2017, **52**, 7008–7016.
33 M. Khatamian, A. A. Khandar, B. Divband, M. Haghighi and S. Ebrahimiasl, *J. Mol. Catal. A: Chem.*, 2012, **365**, 120–127.
34 G. Wang, J. Yang, J. Park, X. Gou, B. Wang, H. Liu and J. Yao, *J. Phys. Chem. C*, 2008, **112**, 8192–8195.
35 V. Jabbari, M. Hamadanian, M. Shamshiri and D. Villagrán, *RSC Adv.*, 2016, **19**, 15678–15687.

36 A. V. Murugan, T. Muraliganth and A. Manthiram, *Chem. Mater.*, 2009, **21**, 5004–5006.

37 Ö. A. Yıldırım, H. E. Unalan and C. Durucan, *J. Am. Ceram. Soc.*, 2013, **96**, 766–773.

38 X. B. Chen and S. S. Mao, *Chem. Rev.*, 2007, **107**, 2891–2959.

39 M. Salavati-Niasari, D. Ghanbari and M. R. Loghman-Estarki, *Polyhedron*, 2012, **35**, 149–153.

40 V. Jabbari, M. Hamadanian, S. Karimzadeh and D. Villagrán, *J. Ind. Eng. Chem.*, 2016, **35**, 132–139.

41 G. Williams, B. Seger and P. V. Kamat, *ACS Nano*, 2008, **2**, 1487–1491.

42 M. Hamadanian, M. Rostami and V. Jabbari, *J. Mater. Sci.: Mater. Electron.*, 2017, DOI: 10.1007/s10854-017-7452-y.

43 H. Zhang, X. Lv, Y. Li, Y. Wang and J. Li, *ACS Nano*, 2010, **4**, 380–386.

44 Z. Q. Li, H. L. Wang, L. Y. Zi, J. J. Zhang and Y. S. Zhang, *Ceram. Int.*, 2015, **41**, 10634–10643.

45 M. Xing, W. Fang, X. Yang, B. Tian and J. Zhang, *Chem. Commun.*, 2014, **136**, 5852–5855.